Robust uncertainty quantification of the volume of tsunami ionospheric holes for the 2011 Tohoku-Oki Earthquake: towards low-cost satellite-based tsunami warning systems

Ryuichi Kanai[1], Masashi Kamogawa[3], Toshiyasu Nagao[4], Alan Smith[2], and Serge Guillas[1]

[1]Department of Statistical Science, University College London, London, UK
[2]Department of Space and Climate Physics, University College London, London, UK
[3]Global Center for Asian and Regional Research, University of Shizuoka, Shizuoka, Japan
[4]Institute of Oceanic Research and Development, Tokai University, Shizuoka, Japan

Correspondence: Ryuichi Kanai (ryuichi.kanai.16@ucl.ac.uk)

Abstract. We develop a new method to analyze the total electron content (TEC) depression in the ionosphere after a tsunami occurrence. We employ Gaussian process regression to accurately estimate the TEC disturbance every 30 s using satellite observations from the GNSS network, even over regions without measurements. We face multiple challenges. First, the impact of the acoustic wave generated by a tsunami onto TEC levels is non-linear and anisotropic. Second, observation points are

5   moving. Third, the measured data is not uniformly distributed in the targeting range. Nevertheless, our method always computes the electron density depression volumes, along with estimated uncertainties, when applied to the 2011 Tohoku-Oki Earthquake, even with random selections of only 5% of the 1,000 GPS Earth Observation Network System receivers considered here over Japan. Also, the statistically estimated TEC depression area mostly overlaps the range of the initial tsunami, which indicates that our method can potentially be used to estimate the initial tsunami. The method can warn of a tsunami event within 15

10   minutes of the earthquake, at high levels of confidence, even with a sparse receiver network. Hence, it is potentially applicable worldwide using the existing GNSS network.

1   Introduction

The damage caused by tsunamis can be devastating. For example, almost 20,000 people died in the tsunami following the 2011 Tohoku tsunami in Japan. One reason for such levels of casualties is that current tsunami height predictions are relatively

15   unreliable, even following an identified earthquake event, and so early warning systems are not as effective as required. Initial sea surface deformations are typically indirectly determined from seismological inversions of the earthquake source. However, some of these early estimates are sometimes much lower than expected: for instance the 2011 Tohoku-oki earthquake initial estimated value of $M_w 7.9$ was used for warnings but the actual magnitude was $M_w 9.1$.

     Research on tsunami warnings has been conducted for a long time, and has undergone remarkable technical evolution with

20   the development of various technologies (Bernard and Titov, 2015; Wächter et al., 2012). For example, in recent years, tsunami warning systems have been developed for tsunamis of seismic origin in and around the Mediterranean Sea (Amato et al., 2021).

Furthermore, the initial tsunami wave cannot be precisely inferred from seismic information alone due to the complexity of the relationship between the earthquake source and the initial wave. For example so-called tsunami earthquakes generate much larger tsunamis than expected from the seismic source, e.g. the Mentawai 2010 tsunami (Lay et al., 2011; Satake et al., 2013), whereas some powerful earthquakes sometimes produce tsunamis much smaller than expected e.g. for the 2005 $M_w 8.6$ Nias earthquake. These deficiencies in the seismic approach become even greater when considering additional contributions to the tsunami wave such as splay faults and submarine landslides not well picked up by seismic monitoring. One could account for the uncertainties in the earthquake source estimates and propagate these to the initial tsunami height in real-time (Giles et al., 2021), but these approaches cannot realistically model in 3-D and in real-time the seabed deformation arising from the earthquake source due to epistemic, computational and observational inadequacies. In addition, in some cases, seismic gaps and coseismic slips do not overlap, which makes tsunami prediction based on seismic data highly difficult (Lorito et al., 2011). Hence, Bernard and Titov (2015) illustrates a more advanced warning system that uses detecting devices such as pressure sensors and predicts tsunami heights using tsunami information. Specifically, observations closely related to the actual generated tsunami wave are more likely to provide more precise warnings. One example is the successful data assimilation of tsunami wave from buoys, with either dense or possibly sparse networks (Tanioka and Gusman, 2018; Wang et al., 2019). Still, some problems remain, such as the high maintenance cost of those devices and avoiding high ocean currents for installation locations (Bernard and Titov, 2015). We explore here the use of real-time satellite data due to its global coverage, low expense, low maintenance, and rapid access.

A path towards accurate warnings is to estimate the Tsunami Ionospheric Holes (TIHs) generated in the ionosphere after the initial tsunami occurrence (Kamogawa et al., 2016). The formation of a TIH, which is a decrease in total electron content (TEC) in the ionosphere, can be explained by the following physical mechanisms (Kamogawa et al., 2016; Shinagawa et al., 2013). First, a displacement of sea surface caused by a tsunami generates acoustic waves that propagate vertically upward and reach the ionosphere. Then, the plasma is moved along the magnetic field by the sound waves and the downward flow is larger than the upward flow partly because the gravity force causes downward motion. The downward plasma causes recombination and ion production is suppressed, resulting in a decrease in TECs, and the depression in TECs is called a TIH. The TIH observed in the ionosphere at the time of the 2011 Tohoku tsunami has been reproduced by performing numerical simulations of this physical phenomenon (Shinagawa et al., 2013; Zettergren et al., 2017; Zettergren and Snively, 2019).

In Japan, the GPS Earth Observation Network System (GEONET), which is a network of more than 1,200 receivers, enables us to observe the behavior of the TEC in the ionosphere with a large number of data points. The most prominent case of the TEC changes in the ionosphere observed by GEONET is the tsunami following the 2011 Earthquake, off of the Pacific coast of Tohoku. By focusing on the changes in the ionosphere after the earthquake and observing the high-frequency component of the TEC fluctuations, Tsugawa et al. (2011) observed a rapid decrease in TEC near the epicenter approximately 7 minutes after the earthquake : the rapid fluctuation of the high-frequency component of TEC was detected as concentric waves that radiated outward, and these concentric waves were confirmed to have had a central point source. Saito et al. (2011a) analyzed the unfiltered TEC fluctuations in which, a significant decrease in

TEC was observed, with an amplitude of up to 5 TECu and an area of 500 km. Similarly, Kakinami et al. (2012) showed that the amplitude of the decrease in TEC exceeds 5 TECu, analyzing the TEC without frequency filtering.

Furthermore, Kamogawa et al. (2016) examined the behavior of the TEC depression in the ionosphere after the tsunami, examining the low-frequency component of TEC in a variety of tsunami cases including the 2011 Tohoku tsunami. They discovered a positive correlation between the initial tsunami height and the rate of TEC depression. It is thus likely possible to detect an initial tsunami by evaluating the magnitude of TIH, which is the reduction of the TEC in the ionosphere. However, it is still challenging to define the scale of TIH, because even if a dense network of GNSS receivers is maintained, such as in Japan, there are areas where the TEC cannot be measured by the network. Moreover, the TEC measurement locations move in the same way as the satellite moves, and those locations are not uniformly distributed within the target range. The shape of the TIH cannot be completely captured from the measurement points alone. In addition, in regions where GNSS observation networks are less dense, the number of available data is even smaller, making it very difficult to detect the TIH confidently.

To overcome these problems, we implement below a statistical method for the analysis of TEC using satellite data, which allows us to estimate TEC values even over areas with no measurements and to evaluate the whole TIH even without a dense measurement network such as GEONET in Japan. Our approach does not make any assumption on the nature of the source of the tsunami. This method enables us to calculate the volume (with uncertainty) of the hole as an assessment of the scale of the TIH, and we propose to use its volume as a measure of the TIH. We believe that estimating the TIH provides a new and important tool for early tsunami warning systems that is independent of seismology.

In section 2, the pre-processing and characteristics of the data are described in detail to ensure that this study is reproducible. In addition, we describe our surface fitting method. In section 3, we present the results of fitting surfaces computed by our new method and the time series analysis of the TIH volume. In section 4, we conclude and mention future possibilities offered by this method.

2 Data and Method

2.1 Data

In this study, TEC is calculated using GEONET data operated by the Geospatial Information Authority of Japan, and the following assumptions are made in processing the data. First, we approximate the F region, which contains many more electrons than other regions in the ionosphere, as a thin layer at an altitude of 300 km because the two effects of the chemical reactions and diffusion are balanced and the electron density is maximized at an altitude of 300 km. The point where the line connecting a GNSS satellite and a receiver intersects with this approximated thin layer is called the ionospheric point (IP). The footprint of the IP to the surface is called the Sub-Ionospheric Point (SIP).

Two radio signals from the GNSS satellites, 1575.42 MHz and 1222.60 MHz, are transmitted to the GNSS receivers, and the propagation time of the radio signals depends on the electron density in the atmosphere. Therefore, the TEC between the GNSS satellites and the GNSS receivers can be estimated from the phase delay of these two types of radio signals. This TEC, which is in the pathway between a satellite and a receiver, is called the slant TEC, noting that in general the line of sight to

the satellite is not vertical. The slant TEC at the time of the earthquake is used as the reference value for the time-series slant

90 TEC data. The time-series slant TEC is defined as the difference between the slant TEC and the reference TEC value for each

satellite receiver pair.

For each time-series slant TEC data, a quadratic fitting is performed by the ordinary least-squares method for data points

from 30 minutes before to 7 minutes after the time of the earthquake to be consistent with the previous study (Kamogawa et al.,

2016). These fitting curves are assumed to represent the time-series slant TEC data as it would have been in the absence of

95 the effect of TEC depression caused by acoustic waves induced by the tsunami because it takes almost 7 minutes for acoustic

waves to reach the ionosphere.

Then, we calculate the difference between the fitting curves and the time-series slant TECs for each case. By multiplying

the time series differences by the cosine of the angle θ between the vertical upward direction and the straight line between the

satellite and the receiver, we obtain ΔvTEC, which is the variation of the vertical component of the slant TEC time series data.

The conceptual diagram of the description of the data processing so far is drawn in Figure 1.
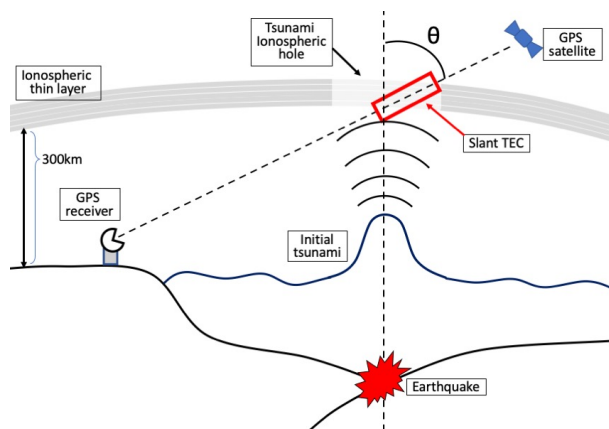
Figure 1. The schematic image of TEC depression detected by a satellite and a receiver.

100

To apply a low-pass filter to this ΔvTEC, we take a 300 seconds backward moving average to obtain the low-frequency

components of ΔvTEC. Since TIH is a hole formed by the decrease of TEC, we want to focus on the decrease of TEC in our

analysis. For this reason, in the following sections, we use the data of which the low-frequency ΔvTEC is less than 1. The

low-frequency ΔvTEC is hereinafter referred as TEC for sake of simplicity.

105 The unit of TEC is TECu, which is 1.0×10^{16} electron m^{-2}. Since the time resolution of the available data is the 30-second

interval, we set the time of the 2011 off the Pacific coast of Tohoku Earthquake occurrence as 6:46:30 (UTC) even though the

exact occurrence time is 6:46:18 (UTC) according to the Japan Meteorological Agency.

In addition, the data includes outliers due to broken receivers. We detected them using the K-nearest neighbor algorithm

(Cover and Hart, 1967), and removed these outliers from the data to be analyzed. The general principle of the K-nearest

110 neighbor algorithm is that for a given data point, k nearest neighbor data sets are identified, and labels are assigned to these k

nearest neighbor data sets and the given data point. Generally, this method requires the definition of the metric for measuring the distance (similarity) between data points, and the number k needs to be chosen as well. Here, simple but effective choices are made: the Euclidean distance is used to measure the similarity and k is defined as the square root of the number of data points in the targeting range.

115 ## 2.2 Robust Fitting Method with Gaussian Process Regression

We analyze data over the area of 10 degrees of latitude and 10 degrees of longitude centered at $38.297°$N and $142.373°$E, the location of the epicenter of the 2011 Tohoku Earthquake as reported by the USGS. Gaussian process (GP) regression (Rasmussen and Williams, 2006) is a method of regressing a function Y (here the TEC as a function of horizontal coordinates) using a flexible nonlinear model based on a set of observed data. A GP is in fact a generalization of the multivariate normal distribu-

120 tion to infinite dimensions: any marginal distribution projected to finite dimensions is multivariate normal. The fitted GP here probabilistically represents all possible TEC surfaces that interpolate (up to a so-called nugget noise level) the observations. We employ here the Matérn kernel with an additional nugget that accounts for some noise about the observations:

$$k_\nu(\boldsymbol{x_p}, \boldsymbol{x_q}) = \frac{2^{1-\nu}}{\Gamma(\nu)} \left(\frac{\sqrt{2\nu}r}{l} \right)^\nu K_\nu \left(\frac{\sqrt{2\nu}r}{l} \right), \tag{1}$$

$$cov(y_p, y_q) = k_\nu(\boldsymbol{x_p}, \boldsymbol{x_q}) + \sigma^2 \delta_{p,q} \tag{2}$$

125 Here, $r = |\boldsymbol{x_p} - \boldsymbol{x_q}|$, K_ν is a modified Bessel function of the second kind, Γ is the Gamma function, ν and l are positive parameters, σ^2 is the variance of the noise (i.e. the nugget), and $\delta_{p,q} = 1$ if $p = q$ and zero otherwise. The Matérn Kernel's smoothness ν generates a GP whose smoothness relates to ν, and should thus be carefully chosen to match the smoothness of the function Y. By setting $\nu = 5/2$, we use a kernel function that is twice differentiable, which, in our analysis, conforms very well to the physical phenomena of TEC reduction.

130 After fitting our GP, the joint distribution of the estimates at any new locations are estimated (with uncertainty) even in areas where there is no measurement data. Here we predict the TEC surface over the area in increments of 0.01 degrees in both latitude and longitude. However, using 1,200 receivers, it takes more than 10 minutes to fit the full data due to costs of $\mathcal{O}(n^3)$ where n is the number of data points.

A stochastic partial differential equation (SPDE) approach using the integrated nested Laplace approximation (INLA) (Lind-

135 gren et al., 2011; Rue et al., 2009) can reduce the cost of fitting the GP. Such an approach not only is faster but has demonstrated that spatial predictions are more accurate, less uncertain and more robust than the standard covariance-based fitting of a GP e.g. when mapping stratospheric ozone (Chang et al., 2015). Exploiting Gaussian Markov random fields (GMRF), the INLA-SPDE reduces costs to $\mathcal{O}(n^{\frac{3}{2}})$ for two dimensions. The crucial point is that a Gaussian spatial process with a Matérn covariance function is the stationary solution to a certain SPDE that can be solved using finite element approaches and approximated using the

140 INLA in the GMRF setting. Nevertheless, some effort must be put into creating a reasonable mesh that solves the SPDE using finite elements, shown in Figure 2. The number of elements in the mesh cannot be too large as the computational burden would become too high, and not too small, as the fitting surface would not be a good approximation of the actual surface.
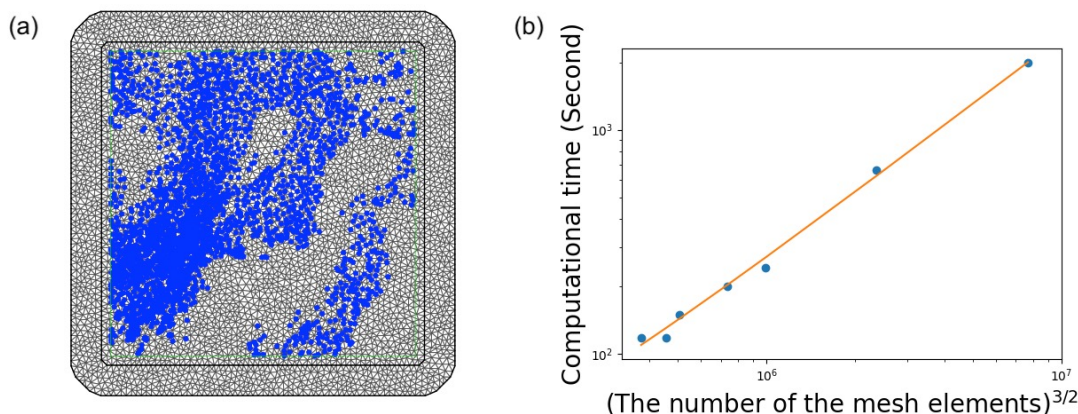
Figure 2. Panel (a) is the mesh elements and observed data, which is plotted with blue marker, at 6:00:00 (UC). The number of mesh elements is about 5,200. Panel (b) is the relationship between computational time and the number of the mesh elementsto the 32 th power. The computation time is the average value of the time at 5:46:30, 6:00:00, 6:08:00, and 6:16:00. The orange solid line is the regression line. The coefficient is 0.000259 and the intercept is 12.044.

Using this INLA-SPDE method with about 5,200 mesh elements, the average computational time to fit the full data and predict the surface in 30-second increments from 5:30:00 to 6:30:00 becomes less than 1 minute, with a standard deviation

145 of less than 5 seconds, whereas the average computational time based on the standard GP regression method is more than 10 minutes, with a standard deviation of more than 2 minutes. The exact values are described in table 1.

Table 1. Computational time for the TEC surface fitting and the TEC value estimation.

	GP regression	INLA-SPDE
Mean time (s)	763.9	43.1
Standard deviation time (s)	151.2	4.5

3   Results

Figure 3 displays the measured TEC data at different times. The red star is the location of the epicenter of the 2011 off the Pacific coast of Tohoku Earthquake and the two large black circles with slanting lines are outliers. It can be seen that the

150 measurement points are moving and are not uniformly distributed in the targeting range, which is from $33.297°$N to $43.297°$N in latitude and from $137.373°$E to $147.373°$E in longitude. Moreover, although it can be confirmed from panels (c) and (d) that the TIH is formed, we argue that a single data point alone such as the minimum TEC value is not enough to evaluate the scale of TIH. Indeed, doing so does not account for the width nor the anisotropy of the TIH. Figure 3 highlights the fact that in order

to properly evaluate the TIH, it is necessary to analyze the data using statistical methods, rather than using the observed data
155   as is.

3.1   Outlier detection

For the two data points that are determined to be outliers by our method, we validate them as outliers as follows. Panel (a) in
Figure 4 is the 3D plot of the captured data by satellites at 6:00:00, and the two red dots are the points identified as outliers.
It is clear that these two outliers have very different values from their neighboring measurement points, but such spikes do not
160   correspond to any genuine physical variations. These points will move further away from the surrounding points over time, and
eventually, the absolute values of the two outliers reach over 50 TECu, which can distort the fitting surface considerably and
prevent proper TIH analysis.

In addition, to validate further, we create a semi-variogram cloud. In the semi-variogram cloud, half the value of the squared
difference between feature values of two data points is plotted against the difference in geographical space between the two data
165   points. Panel (b) shows the semi-variogram cloud of the data at 6:00:00 (UTC), where the red points are associated with points
considered as outliers by our method. We can see that these two points present extremely different values when compared to
the other measurement points. This correspond to a clear lack of correlation between these two points and the rest of the data
set.

Our method identifies the receivers that correspond to the outliers. In this case, these outliers are observed by the receiver
170   960588 and 950175 respectively. According to the Geospatial Information Authority of Japan, either the antennas of the
receiver or the receiver itself was replaced by a new one in the following year of the 2011 Tohoku-Oki earthquake.

In the analysis, it is inappropriate to include observations measured by receivers that would have been broken. Therefore,
the exclusion of these outliers is essential to the TIH analysis, and hence all the analyses in this study are implemented after
removing the outliers.

175   ### 3.2   Surface fitting with full data

Figure 5 shows that measured TEC data, its fitting surface and confidence interval, and 2D mapping for both full data and
sparse data at 6:08:30 (UTC). Although Figure 5 panel (a) shows that the observed TEC decreases near the epicenter, which is
shown using a red star mark, the position where it decreases the most and the range of the depression cannot be described in
detail due to the limited number of data points. In addition, the degree of TEC decrease in panel (a) and the three-dimensional
180   plot of the TEC depression represented by blue dots in panel (c) show that the TEC values gradually changes from 0 in the
area where TEC continues to be stable to the minimum value in the region where it is decreasing the most. These facts indicate
that, in the evaluation of TIH, it is necessary to estimate the values of TECs where no captured data exists, in order to use a
measure that can take the overall variation into account rather than using a single data point.

Here, we present our method's success in surface fitting with uncertainty as expressed in panel (c) and (e) in which respec-
185   tively the surface and confidence interval are depicted with red and green colours. The fitted surface in panel (c) is an almost
perfect fit to the TEC data observed by the satellites. We can thus confirm that the TEC values on the surface do not change
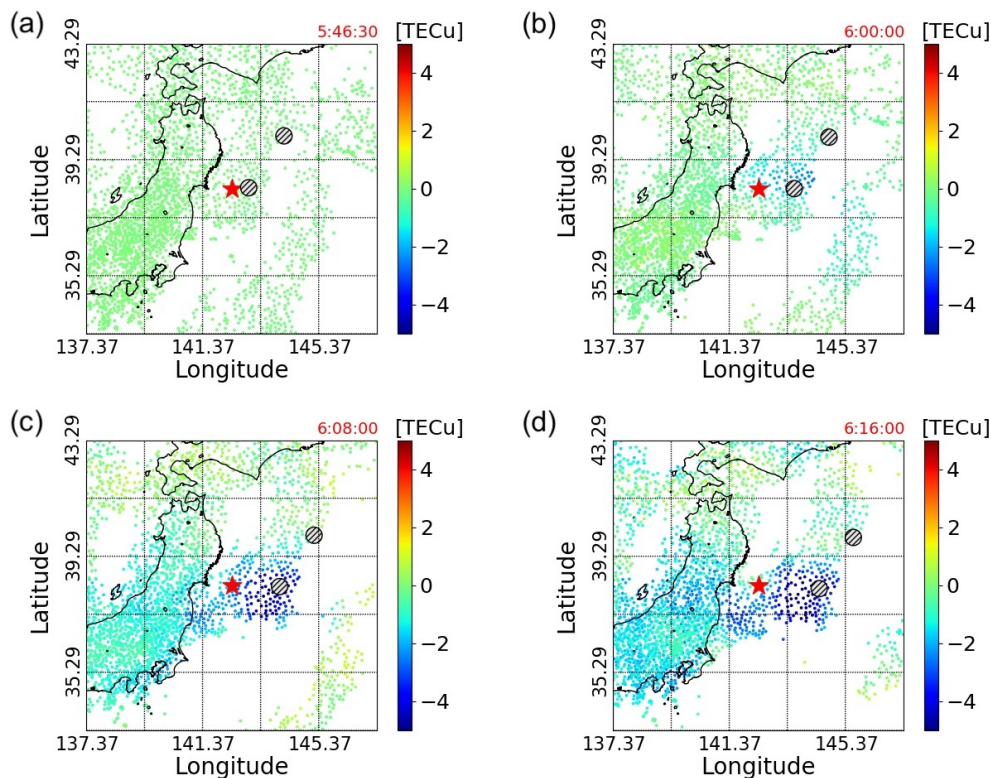
Figure 3. The red star is the epicenter and the two large black circles are the outliers. Panel(a), (b), (c), and (d) are the TEC data measured by GNSS network at 5:46:30, 6:00:00, 6:08:00, and 6:16:00 (UTC) respectively. 5:46:30 was the time of the earthquake occurrence.
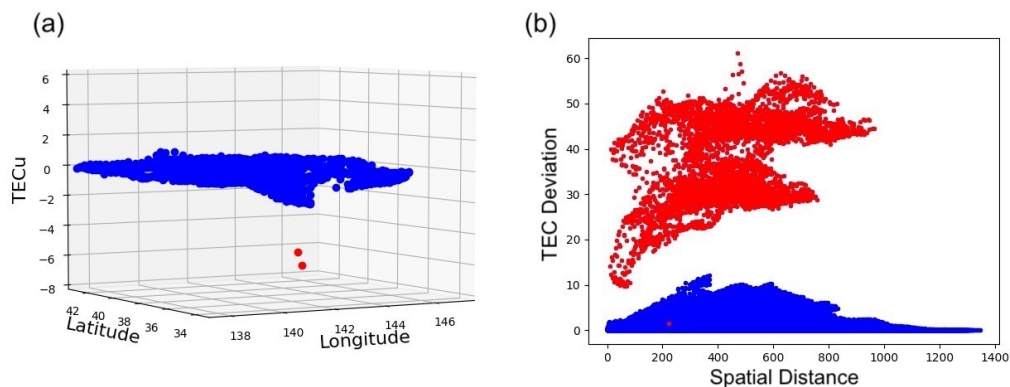
Figure 4. Panel (a) is the 3D plot of the captured data. The two red dots are outliers identified by our method. Panel (b) is the semi-variogram cloud of the data. In both (a) and (b), the data depicted and analyzed is captured by satellites at 6:00:00 (UTC).
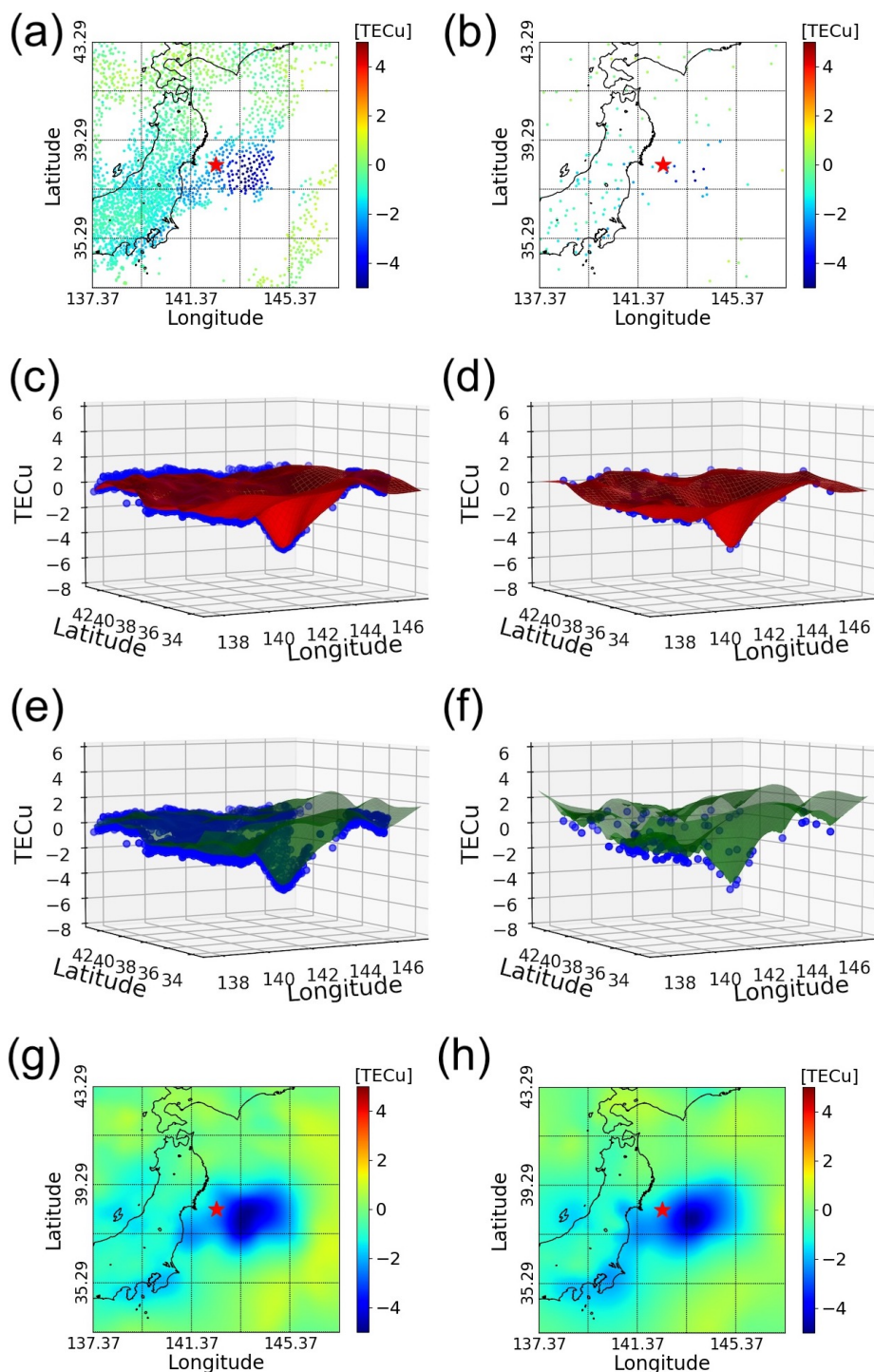
Figure 5. Left-hand side is for the full data and right-hand side is for the sparse data using only 5% of the GEONET receivers. (a) and (b) are measured TEC data. (c) and (d) are measured TEC data (blue dots) and the fitting surface (red surface). (e) and (f) are measured TEC data (blue dots) and 99% one-sided confidence interval of the fitting surface (green surface). (g) and (h) are 2D projection of the fitting surface. All plots are for data at 6:08:30 (UTC). The fitting surface is computed using the INLA-SPDE method.

linearly from the stable area to its minimum. This fact indicates that the TEC oscillation, which is thought to be the effect of high-frequency components (Tsugawa et al., 2011), remains even after implementing the data pre-processing, which is low pass filter. Panel (g), which is the 2D projection of the fitting surface, shows that our method enables us to estimate the TEC

190 values with a fine granularity even over the region where the data is not detected by the GNSS satellites and receivers. The estimated values are computed and displayed in increments of 0.01 degrees in latitude and longitude. The result shows that our method can capture the TIH anisotropic structure (Zettergren and Snively, 2019). In addition, the 2d projection result shows that the epicenter of the earthquake and the place where the minimum TEC value is obtained are explicitly different. It is also found that the shape and region of the TIH region are almost the same as those of the initial tsunami shown by the simulation

195 Saito et al. (2011b).

3.3 Surface fitting with sparse data

Unlike the case of full data displayed in panel (a), it can be clearly seen from panel (b) that the number of data points in the sparse data case is not sufficient to entirely analyze TIH, where 95% of the GNSS receivers are randomly removed from

200 the observed data. This situation is highly possible in areas where a dense network of GNSS satellites and receivers has not been installed and hence the appropriate analysis for TIH is almost impossible from the captured data. Nevertheless, our new analysis method can overcome this sparse data problem effectively.

In panel (d) and (f), the fitting surface, its confidence interval, and almost 5% of captured data are depicted by a red surface, a green surface, and blue dots respectively. The uncertainty naturally increases by comparing panel (f) with panel (e) since the

205 number of data points is smaller than that of the original data. Despite the extremely small number of data points, our method is successful in surface fitting and uncertainty evaluation.

2D projection of the fitting surface with sparse data, in panel (h), shows that the location and range of the TIH are adequately estimated and consistent with those of the full data case shown in panel (g). To be more specific, our method is able to estimate the anisotropic TIH, which is consistent with the location and shape of the initial tsunami. These results demonstrate that

210 our new method based on GP regression overcomes the sparse data problem by implementing surface fitting that adequately estimated TEC variation with uncertainty and captured TIH shape.

3.4 TIH expansion

Since we are able to estimate all the TEC variations in the target area, we analyze the shape of TIH in detail using the observed data. Figure 6 displays the distribution of TEC below different levels at different times. Specifically, in panels (a1) to (a3),

215 the shapes of TIH limited to TEC values of -2 or less are drawn at 6:08:00, 6:12:00, and 6:16:00 (UTC). Similarly, in panels (b1) to (b3) and panels (c1) to (c3), the shapes of TIHs with TEC values of -3 or less and -4 or less, respectively, are drawn. In these panels, the eight triangles, which are colored in pink, orange, brown, black, red, grey, yellow, and green respectively, are the points where the TIH below the specified level is the most expanded, located in the south, north, west, east, northeast, southeast, northwest, and southwest directions from the tsunami source. The tsunami source was set to 38°N and 143.4°E,

220 which was calculated in a previous study (Kamogawa et al., 2016) as the average of tsunami sources obtained from previous research papers.

As shown in panels (a1) to (a3), the region with TEC less than -2 can be seen to expand less to the north direction than the other directions. In addition, a TEC decrease isolated from the TIH directly above the tsunami can be seen in the southwest direction. As an overall trend, it can be said that the expansion of TIH in the east and southwest directions is more pronounced

225 than in the other directions.

However, when we observed the behavior of panels (b1) to (b3), where the value of TEC is less than -3, we found that the expansion of TIH is different from that of TIH with a TEC value less than -2 described in panels (a1) to (a3). First of all, the area of TIH has not expanded so much as that of TIH with TEC less than -2. In addition, the southwestward expansion is not as large as that of TIH in panels (a1) to (a3). For example, the eastward expansion appears to be the most pronounced, and also

230 the northward expansion is less pronounced than in other directions, which are similar characteristics.

In the case of TIH with TEC less than -4, shown in panels (c1) to (c3), the westward expansion is smaller than the expansion in the other directions. In addition, the TIH center does not remain directly above the vicinity of the tsunami source, but appears to be moving to the southeast. It can also be seen that the region where TEC is less than or equal to -4 does not expand significantly during the period of 20 to 30 minutes after the earthquake, but it does not shrink significantly either. In other

235 words, when we focus on the TEC values below -4, the shape of the TEC is almost stable.

3.5   TIH expansion distance in each direction

From Figure 6, it can be inferred that the time evolution of the shape of the region with small TEC variation and that with large TEC variation do not necessarily coincide. To investigate this point in more detail, we analyze the graphs with the distance in km plotted by time for the most expanded points in the eight directions from the tsunami source. Here, the distance is

240 computed by Hubeny's distance formula. In Figure 7, the distance between the most expanded point in the eight directions and the tsunami source when the TEC value is -2 or less (panel a), when the TEC value is -3 or less (panel b), and when the TEC value is -4 or less (panel c) are drawn, respectively. The eight directions are the same as in Figure 6, and the color coding for each is also the same.

In panel (a), it can be seen that the expansion in the northeast direction progresses earlier than other directions. A little

245 later, the eastward expansion continues to progress, and finally the eastward expansion progresses more than the northeastward expansion. The expansion to the south, after increasing for some reason, begins to decrease, and then continues to expand again. Eventually, it will be as large as the eastward expansion. The westward expansion is a discontinuous movement due to the definition of distance and direction in this analysis. Specifically, as depicted in panels (a2) and (a3) of Figure 6, the region with TEC less than -2 has a special shape in the western direction, and the distance in this direction tends to be more

250 discontinuous than the distances in other directions. What is noteworthy is the expansion of the distance in the north and northwest directions. The progress of the distances in these directions is clearly smaller than those in other directions. For example, compared to the expansion in the east direction, the distance in the north and northwest directions is less than half.
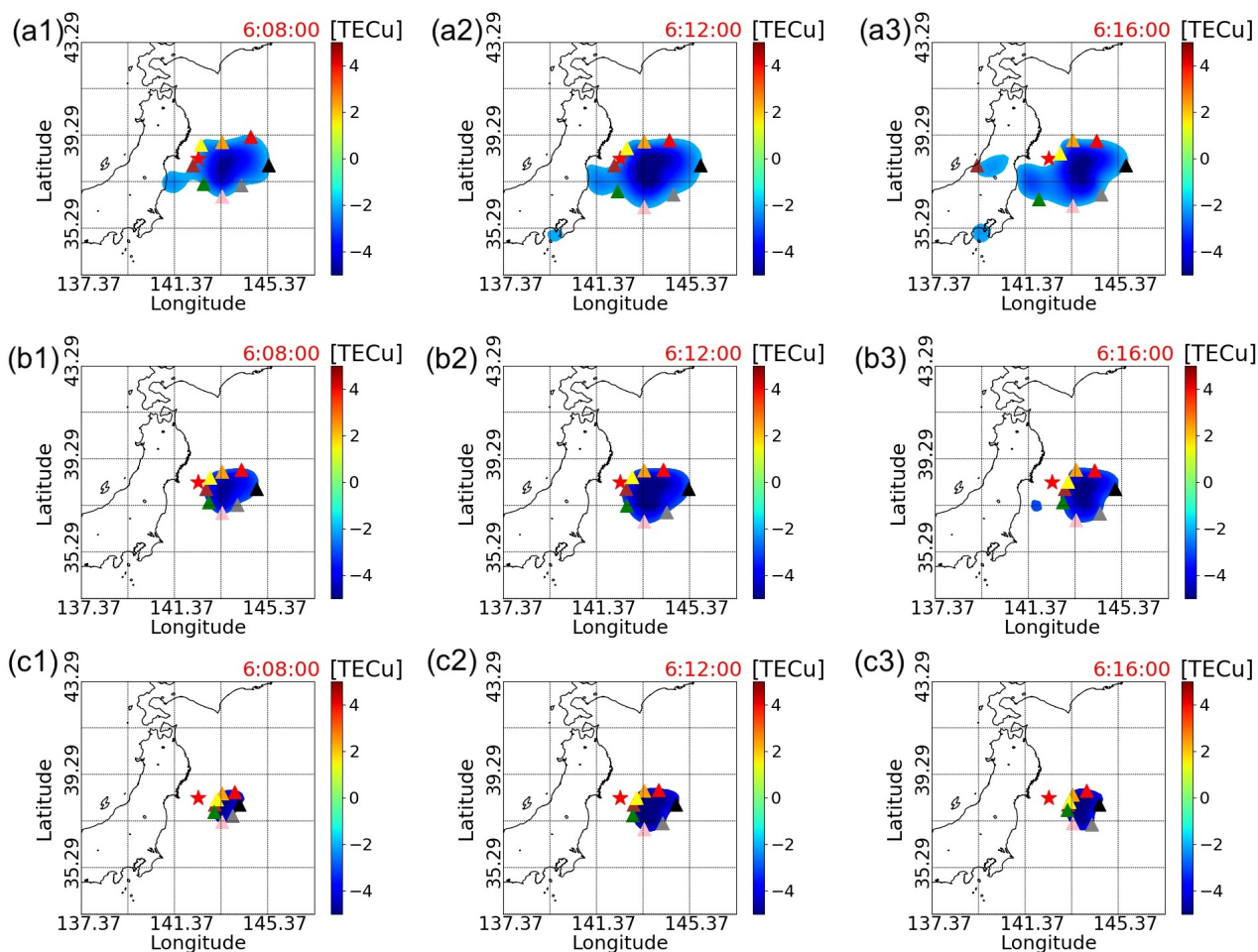
Figure 6. Tsunami Ionospheric Hole expansion: (a1)-(a3) are plots of TIH with TEC less than or equal to -2. (b1)-(b3) and (c1)-(c3) are less than or equal to -3 and -4 respectively. These plots are at 6:08:00, 6:12:00, and 6:16:00 (UTC). The eight triangles are south, north, west, east, northeast, southeast, northwest, and southwest directions from the tsunami source, respectively. The colors are pink, orange, brown, black, red, grey, yellow, and green respectively. The red star mark is the location of the epicenter.

In Panel (b), the time evolution of the distances in all directions appears to be continuous. In this case, too, the expansion to-ward the northeast progresses in the initial stage, but then the expansion toward the east progresses significantly. The expansion

255 in the south direction can be said to be slower than that of the two directions mentioned above, but it eventually expands by the same distance as that in the east direction. The southeast direction shows a similar trend to the expansion in the south direction, and although the initial expansion is not so large, the final value is large. It can be seen that the north and southwest directions do not expand as much even at the beginning, and then remain in a stable state with almost the same value over time. The northwest direction, as with panel (a), is one of the directions that does not expand the most. The most significant difference

260 between Panel (b) and Panel (a) is the expansion in the west direction. In Panel (a), the distance in the west direction expands discontinuously and finally reaches the highest value. On the other hand, in Panel (b), the distance in the west direction is the smallest in almost all time periods.

In panel (c), the time at which the image begins to expand is greatly delayed because the threshold is set even smaller than in panels (a) and (b). Initially, the expansion in the northwest and south directions is significant, and as time passes, the expansion

265 in the east direction becomes the largest. Eventually, the distance in the southeast direction becomes larger than the distances in the other directions at the end of the period, but its maximum value is smaller than the value recorded by the east direction around 6:10:30 (UTC). The expansions in the north and southwest directions show almost the same development. For the northwest and west directions, as in panel (b), only the smallest expansion is shown during the period.

3.6 TIH overlapping with initial tsunami

270 Unlike the high-frequency component of the TEC variation (Tsugawa et al., 2011), the low-frequency component of the TEC variation displays large drops in its values and remains fixed within a region, as shown in Figure 6. Since this TEC reduction is caused by the initial tsunami, staying in the same location is theoretically correct. As shown in Figure 8, the initial tsunami estimated by Saito et al. (2011b) using inversion analysis mostly overlaps with the TIH where the TEC reduction is large. Although there have been studies to estimate the tsunami source using TEC fluctuation data, these estimate the tsunami source

275 as a point (Liu et al., 2019). We show here for the first time that our method of estimating the entire TIH by Gaussian process regression can be used to estimate the initial tsunami region as shown in Figure 8. In the case of TEC values less than -3 shown in Panel (a1), (a2), and (a3), the TIH almost overlaps the initial tsunami areas, while (b1), (b2), and (b3) where TEC values less than -4 shows TIH stays within the initial tsunami region.

3.7 TIH volume computation

280 Figure 9 shows the time series of the TIH volume, which is computed by trapezoidal quadrature method for the region where the TEC estimated by the surface fitting has a negative value. In other words, the volume between the flat surface, that is the TEC values are equal to 0, and the fitting surface which has negative value is calculated.

The main effect by acoustic waves induced by the initial tsunami is that the reduction of TEC in the ionosphere by moving the plasma along the magnetic field and causing recombination. More specifically, although there are regions where the TEC

285 increases due to complex physical mechanisms, the magnitude of the initial tsunami can be assessed by focusing on the decrease
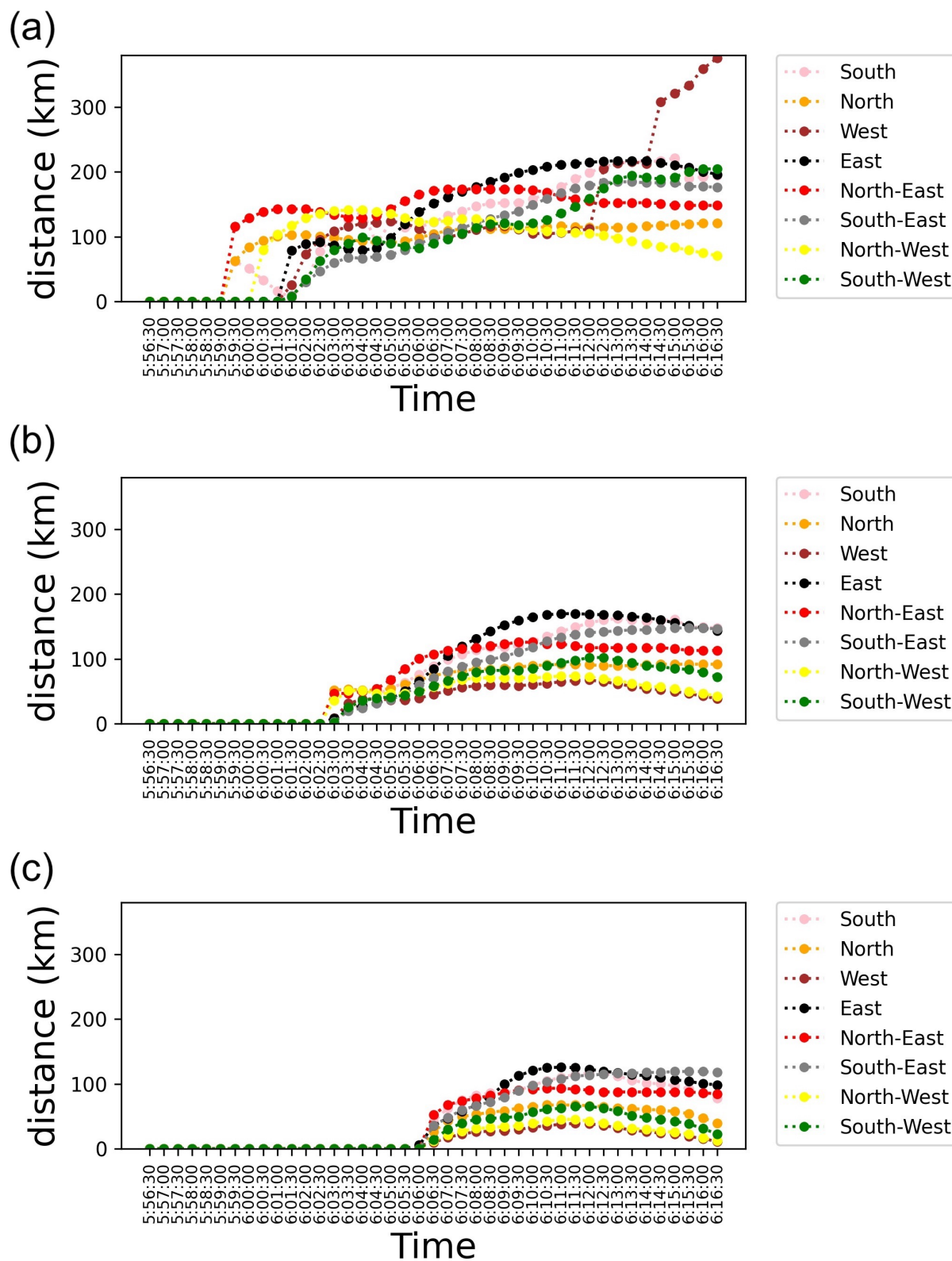
Figure 7. Tsunami Ionospheric Hole expansion: (a) is the time series of distance from the tsunami source in 8 directions for TIH with TEC less than or equal to -2. (b) and (c) are the time series of distance with TEC less than or equal to -3 and -4 respectively.
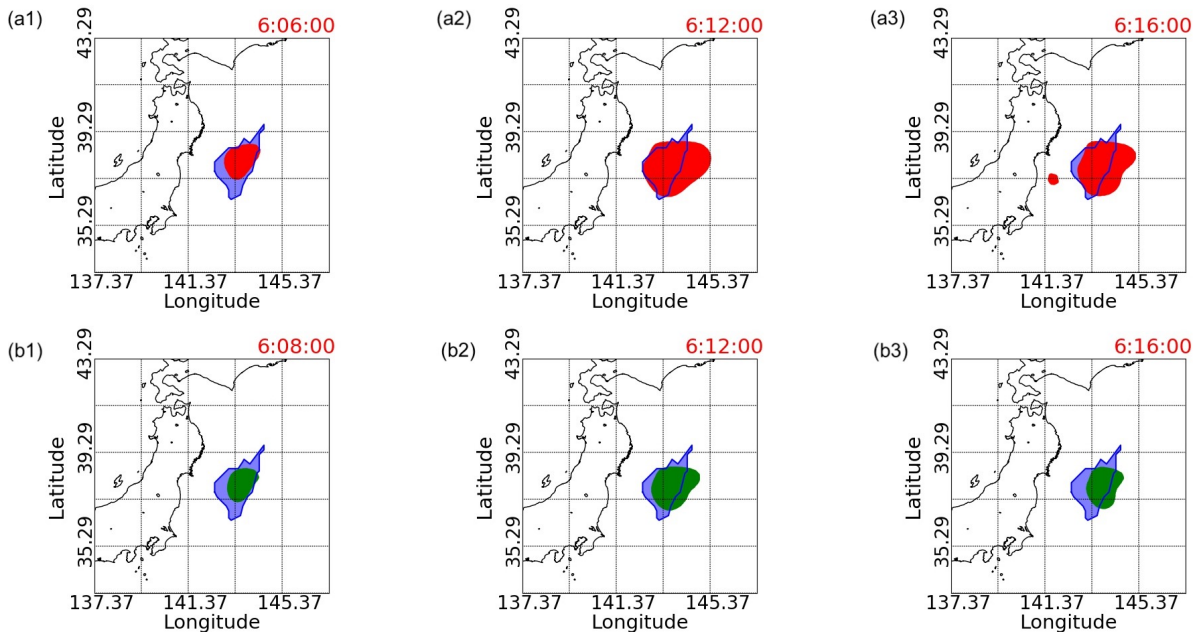
Figure 8. The initial tsunami and TIHs with TEC values less than -3 or -4. The blue area is the simulated initial tsunami by inversion analysis with 130 small basis functions implemented by Saito et al. (2011b). In Panel (a1), (a2), and (a3), the red areas are TIHs with TEC less than -3, while the green areas in Panel (b1), (b2), and (b3) illustrate TIHs with TEC less than -4. Panel (a1) and (b1) are snapshots at 6:08:00 (UTC), (a2) and (b2) are at 6:12:00 (UTC), and (a3) and (b3) are at 6:16:00 (UTC).

in the TEC. Therefore, the volume of the region with negative TEC value is considered to be related to the magnitude of the initial tsunami.

In panel (a), the surface fitting is implemented with simple GP regression, while the INLA-SPDE method is applied to the GP regression process in panel (b). The solid lines in panel (a) and (b) in Figure 9 display the TIH volumes computed for the full data and the dashed lines are for the sparse data. In the case of the sparse data, we repeat 10 times the random selection of 5% of the receivers and the GP regression to fit the surfaces, and then calculate the average value using each computed volume. This iterative process is intended to exclude a possible influence of the random seed used in the sparse data selection on the results. As shown in Figure 3, the measurement points are moving and not uniformly distributed in the targeting range. Still, the time series of the computed TIH volumes looks continuous, as shown in panel (a) and (b) in Figure 9.

The volume of the TIH begins to increase almost 10 minutes after the earthquake occurrence and continues to increase until about 28 minutes after the earthquake shown in Figure 9 (a) and (b). Past study of actual post-earthquake TEC variation data has confirmed that the percentages of TEC depressions for huge simulated tsunami reach almost 40 times as large as those for smaller simulated tsunami (Kamogawa et al., 2016). Although it is impossible to understand the time evolution of TIH volume in advance since no study has considered and analyzed the entire TEC variation in the targeting range under the extremely
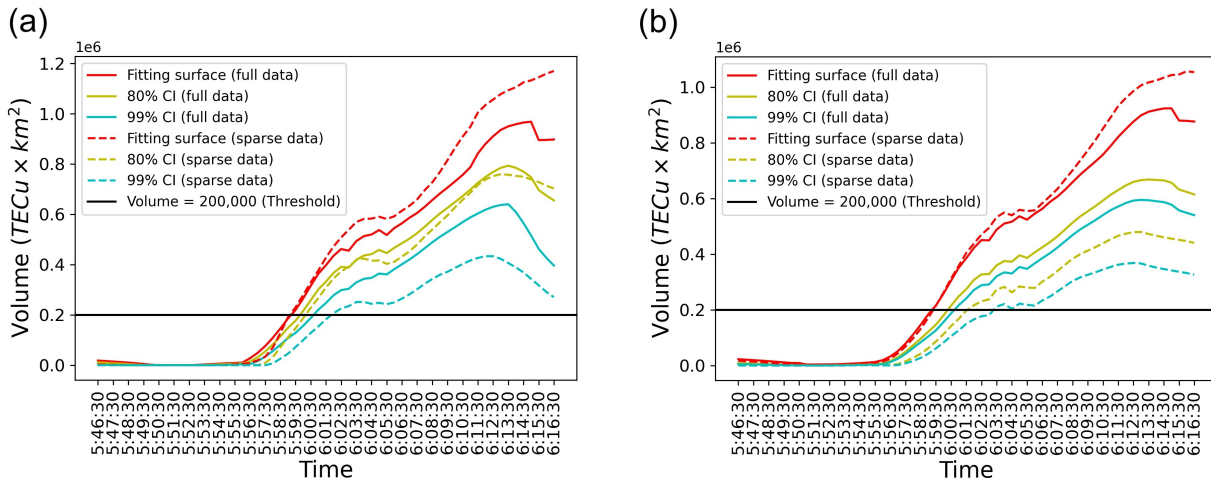
Figure 9. The time series of TIH volume for full data and sparse data with one-sided confidence interval. The red solid line is the volume calculated with fitting surface for full data.The solid yellow line and the solid blue line are one-sided 80% CI and 99% CI respectively. The dashed lines are for sparse data with only 5% of receivers. The horizontal black line is a provisional threshold. (a) The TEC surface is computed based on GP regression. (b) The TEC surface is computed based on GP regression using the INLA-SPDE method.

300   complex TIH mechanism and our new method is applied to only one tsunami case, it is a sufficiently conservative estimate that the threshold is set at about 10-20% of the maximum TIH volume according to the aforementioned previous study. Therefore, if the volume exceeds this threshold, it is reasonable to draw the conclusion that a huge tsunami is being generated. In this analysis, a provisional threshold is set at 200,000 TECu$\times$km^2.

     In the case of the full data, both panels show that the volumes calculated from the fitting surface (but not accounting for

305   uncertainties in the approximation) reach the threshold 1 and 2 minutes earlier respectively than the volumes of 80% and 99% CI. Similarly, in the case of the sparse data, the time difference is about 2 and 4 minutes respectively to reach the threshold for the volumes computed from the fitting surface and both CIs. It means that thanks to our uncertainty computations, making sure that a warning is at a high level of confidence, based on data, of either 80% or 99% results in delays for advisories of only respectively 1-2 or 2-4 minutes.

310   The warning system based on this method is highly feasible because the surface fitting and the estimation of the TEC values for the full data can be processed in less than a minute based on the INLA-SPDE method. However, in the case of the sparse data fitting, our implementation of the INLA-SPDE method sometimes fails due to the geometric meshing optimised for larger data sets, naturally where the benefit of this method is. Nevertheless, the robustness and feasibility of this method never deteriorate because it is possible to compute the surface and estimated values in less than 10 seconds for the sparse data case based on the

315   standard GP regression method.

     Our method is the first to demonstrate that we can calculate the volume of TIHs accurately in real-time and use it as a measure of TIHs even when only a limited number of measurement points are available. In addition, the time series of the

volumes obtained from the surface by points on the 80% and 99% one-sided confidence intervals (CIs) of the TEC values are also plotted in Figure 9.

320

4   Conclusions

In this paper, we compute the volume of the ionospheric depression generated by a tsunami, in real time, and with enough confidence to issue warnings. The surface fits the TEC data using a Gaussian process regression after removing outliers. It enables us to estimate the TEC values over the entire target area. Furthermore, uncertainty can be properly evaluated for the

325 estimated value of TEC according to the density of observations.

The TIH captured by our method is located east of the epicenter. This is consistent with the initial tsunami estimated by the inversion analysis of the waveforms being east of the epicenter (Saito et al., 2011b). Also, the estimated TIH almost overlaps with the estimated initial tsunami area. In the ionosphere, the anisotropic conductance and geomagnetic field directions theoretically cause ionospheric currents to have complex shapes (Zettergren and Snively, 2019). We concretely show here that

330 the estimated TIH can be anisotropic using observed TEC data and a statistical approach.

As shown in our results, this new method is robust as it works in situations where measurements are not uniformly distributed and moving, TIHs display anisotropy, and even if the number of observed data points is sparse. Since our estimates of the shape of the anisotropic TIHs reflect the signature of the initial tsunami wave, we demonstrate that using one specific data point such as the minimum observed value as a scale of a TIH (Kamogawa et al., 2016) is insufficient to characterise the initial wave. Our

335 computation of the volume of TIHs as a measure to assess the scale of TIHs takes fully into account the spatial variations of the TEC depression generated by the tsunami over the domain, including any anisotropy.

In addition, although there have been papers referring to TIH based on observational data (Kakinami et al., 2012; Kamogawa et al., 2016), it was impossible to give a detailed explanation of the temporal variation of TIH in those papers due to data limitations. Using our method, however, the detailed TIH expansion anaylsis based on different thresholds becomes possible.

340 One of the findings is that the way in which the region with small TEC variation expands is dramatically different from that with large TEC variation expands. In our study, it is confirmed that the northward expansion is smaller than the southward expansion, no matter at which threshold level the TIH expansion is checked. This is consistent with the outcomes in previous studies Heki and Ping (2005) that in the northern hemisphere, the interaction of the geomagnetic field with the movement of charged particles in acoustic waves may have attenuated northward propagating. This result is also consistent with the simulated

345 results of previous studies using 3-dimensional simulations Zettergren et al. (2017); Zettergren and Snively (2019), where the TEC decrease in the south direction was larger than that in the north direction. While the results of the 2D simulations did not show a relatively large decrease in TEC to the south Shinagawa et al. (2013), the 3D simulations did Zettergren et al. (2017); Zettergren and Snively (2019), and we have demonstrated this through statistical analysis based on satellite captured data.

As for the high-frequency component of the TEC variability, past studies (Saito et al., 2011a) analyzing observational data

350 have confirmed that the eastward propagation of the TEC fluctuation is faster than the westward propagation. Although our

analysis is focused on the low-frequency component, we have confirmed for the first time that the westward expansion of TIH with TEC less than -3, estimated by this new method, is less rapid than the eastward expansion. However, no similar simulation results have been reported so far for the asymmetry in the east-west direction found in our analysis based on the measured data. Furthermore, the westward expansion observed for TEC values below -2 cannot be satisfactorily explained

355   by the relevant previous studies, and further detailed analysis is needed. Previous papers based on observation data without imposing frequency filters mention that the TIH stops just above the tsunami source, but a more detailed analysis in our study shows that TIH with a threshold of TEC variation below -2 expands over time. The TIH separated by each of these thresholds overlaps with the initial tsunami region calculated by Inversion analysis (Saito et al., 2011b). In the previous study using TEC observational data Liu et al. (2020), tsunami source is analysed, but the result is a point estimation. On the other hand, our

360   method can estimate tsunami region because it is possible to cover all the targeting area.

     There have been attempts to construct tsunami early warning using TEC variations. Liu et al. (2019) demonstrates that the location of the tsunami source can be estimated from 10 IPs by observing TEC variations with a high-pass filter using methods that considers the propagation speed such as the circle method, the ray-tracing technique, and the beam-forming technique. However, these methods only identify the tsunami source with uncertainty and do not take into account the scale and range of

365   the initial tsunami. As larger initial tsunamis cause larger decreases in TEC (Astafyeva et al., 2013; Kamogawa et al., 2016), if a TIH volume reaches a certain threshold, then it indicates that a large-scale initial tsunami has occurred. Therefore, using our method, it is possible to build an early warning system that issues a tsunami warning when the volume of the TIH exceeds a certain threshold, taking uncertainty into consideration. In our analysis, we set a provisional threshold at $200,000\ \mathrm{TECu}\times\mathrm{km}^2$, and it is clear that the volumes calculated using both full data and sparse data exceed the threshold within 15 minutes after

370   the earthquake occurrence, or sooner with a lower threshold. Even carrying out the computations in the most exacting case, using 99% confidence intervals and sparse data (5% of the total observations) only delays the warning by around 4 minutes. We anticipate that more numerical work, more physical understanding of possible natural levels of TEC variations, and more data analysis will be required to establish more finely the thresholds at which advisories can be issued, and thus shorten the advisories to possibly 10 minutes or so. Although, in some cases, tsunamis reach the coast very fast, to apply our method

375   there must be a minimum window of almost 10 minutes between generation and arrival. However, this is perfectly valid for tsunami hazard assessment over populous regions with larger arrival times, as for example tsunami hazard assessment in the city of Victoria, British Columbia, from a tsunami generated in the Cascadia subduction zone (Salmanidou et al., 2021). Our implementation on the 2011 Tohoku Earthquake in Japan demonstrates that our method works well there. Hence it is very likely that this method can be applied to tsunamis around the world, caused by any kind of sources. This may enable the construction

380   of a robust worldwide tsunami early warning system using the volume of TIHs as an index.

Data availability. GPS data was provided by Geospatial Information Authority of Japan at ftp://terras.gsi.go.jp/. Currently, the data can be purchased from the Japan Association of Surveyors http://www.jsurvey.jp/eng.htm.

Author contributions. RK: Conceptualization, Data curation, Formal analysis, Investigation, Methodology, Visualization, and Writing original draft. MK: Funding acquisition, Data curation, and Software. TN: Funding acquisition, Data curation, Software, Review, and Editing. 385 AS: Supervision, Methodology, Review, and Editing. SG: Conceptualization, Supervision, Funding acquisition, Investigation, Review, and Editing.

Competing interests. The authors declare that they have no conflict of interest.

Acknowledgements. The authors acknowledge the use of the UCL Myriad High Performance Computing Facility (Myriad@UCL), and associated support services, in the completion of this work. RK is supported by the Japan Student Services Organization. This research was 390 partly supported by the Ministry of Education, Culture, Sports, Science and Technology through a Grant-in-Aid for Scientific Research (B) No. 17H02058, 2017-2020 (MK) and Earthquake Research Institute (University of Tokyo) cooperative research program (MK and RK). SG was supported by the Alan Turing Institute project "Uncertainty Quantification of complex computer models. Applications to tsunami and climate" under the EPSRC grant EP/N510129/1 and "Real-time Advanced Data assimilation for Digital Simulation of Numerical Twins on HPC" under the EPSRC grant EP/T001569/1.

References

Amato, A., Avallone, A., Basili, R., Bernardi, F., Brizuela, B., Graziani, L., Herrero, A., Lorenzino, M. C., Lorito, S., Mele, F. M., et al.: From Seismic Monitoring to Tsunami Warning in the Mediterranean Sea, Seismological Research Letters, https://doi.org/https://doi.org/10.1785/0220200437, 2021.

Astafyeva, E., Shalimov, S., Olshanskaya, E., and Lognonné, P.: Ionospheric response to earthquakes of different magnitudes: Larger quakes perturb the ionosphere stronger and longer, Geophysical Research Letters, 40, 1675–1681, https://doi.org/https://doi.org/10.1002/grl.50398, 2013.

Bernard, E. and Titov, V.: Evolution of tsunami warning systems and products, Philosophical Transactions of the Royal Society A: Mathematical, Physical and Engineering Sciences, 373, 20140 371, https://doi.org/https://doi.org/10.1098/rsta.2014.0371, 2015.

Chang, K.-L., Guillas, S., and Fioletov, V.: Spatial mapping of ground-based observations of total ozone, Atmospheric Measurement Techniques, 8, 4487–4505, https://doi.org/https://doi.org/10.5194/amt-8-4487-2015, 2015.

Cover, T. and Hart, P.: Nearest neighbor pattern classification, IEEE transactions on information theory, 13, 21–27, https://doi.org/https://doi.org/10.1109/TIT.1967.1053964, 1967.

Giles, D., Gopinathan, D., Guillas, S., and Dias, F.: Faster than real time tsunami warning with associated hazard uncertainties, Frontiers in Earth Science, 8, 560, https://doi.org/https://doi.org/10.3389/feart.2020.597865, 2021.

Heki, K. and Ping, J.: Directivity and apparent velocity of the coseismic ionospheric disturbances observed with a dense GPS array, Earth and Planetary Science Letters, 236, 845–855, https://doi.org/https://doi.org/10.1016/j.epsl.2005.06.010, 2005.

Kakinami, Y., Kamogawa, M., Tanioka, Y., Watanabe, S., Gusman, A. R., Liu, J.-Y., et al.: Tsunamigenic ionospheric hole, Geophysical Research Letters, 39, https://doi.org/https://doi.org/10.1029/2011GL050159, 2012.

Kamogawa, M., Orihara, Y., Tsurudome, C., Tomida, Y., Kanaya, T., Ikeda, D., et al.: A possible space-based tsunami early warning system using observations of the tsunami ionospheric hole, Scientific reports, 6, 37 989, https://doi.org/https://doi.org/10.1038/srep37989, 2016.

Lay, T., Ammon, C. J., Kanamori, H., Yamazaki, Y., Cheung, K. F., and Hutko, A. R.: The 25 October 2010 Mentawai tsunami earthquake (Mw 7.8) and the tsunami hazard presented by shallow megathrust ruptures, Geophysical Research Letters, 38, https://doi.org/https://doi.org/10.1029/2010GL046552, 2011.

Lindgren, F., Rue, H., and Lindström, J.: An explicit link between Gaussian fields and Gaussian Markov random fields: the stochastic partial differential equation approach, Journal of the Royal Statistical Society: Series B (Statistical Methodology), 73, 423–498, https://doi.org/10.1111/j.1467-9868.2011.00777.x, 2011.

Liu, J.-Y., Lin, C.-Y., Tsai, Y.-L., Liu, T.-C., Hattori, K., Sun, Y.-Y., and Wu, T.-R.: Ionospheric GNSS total electron content for tsunami warning, Journal of Earthquake and Tsunami, 13, 1941 007, https://doi.org/https://doi.org/10.1142/S1793431119410070, 2019.

Liu, J.-Y., Lin, C.-Y., Chen, Y.-I., Wu, T.-R., Chung, M.-J., Liu, T.-C., Tsai, Y.-L., Chang, L. C., Chao, C.-K., Ouzounov, D., et al.: The source detection of 28 September 2018 Sulawesi tsunami by using ionospheric GNSS total electron content disturbance, Geoscience Letters, 7, 1–7, https://doi.org/https://doi.org/10.1186/s40562-020-00160-w, 2020.

Lorito, S., Romano, F., Atzori, S., Tong, X., Avallone, A., McCloskey, J., Cocco, M., Boschi, E., and Piatanesi, A.: Limited overlap between the seismic gap and coseismic slip of the great 2010 Chile earthquake, Nature Geoscience, 4, 173–177, https://doi.org/https://doi.org/10.1038/ngeo1073, 2011.

Rasmussen, C. E. and Williams, C. K. I.: Gaussian Processes for Machine Learning, MIT press Cambridge, MA, https://doi.org/https://mitpress.mit.edu/books/gaussian-processes-machine-learning, 2006.

Rue, H., Martino, S., and Chopin, N.: Approximate Bayesian inference for latent Gaussian models by using integrated nested Laplace approximations, Journal of the royal statistical society: Series b (statistical methodology), 71, 319–392, https://doi.org/https://doi.org/10.1111/j.1467-9868.2008.00700.x, 2009.

435 Saito, A., Tsugawa, T., Otsuka, Y., Nishioka, M., Iyemori, T., Matsumura, M., et al.: Acoustic resonance and plasma depletion detected by GPS total electron content observation after the 2011 off the Pacific coast of Tohoku Earthquake, Earth, planets and space, 63, 863–867, https://doi.org/https://doi.org/10.5047/eps.2011.06.034, 2011a.

Saito, T., Ito, Y., Inazu, D., and Hino, R.: Tsunami source of the 2011 Tohoku-Oki earthquake, Japan: Inversion analysis based on dispersive tsunami simulations, Geophysical Research Letters, 38, https://doi.org/https://doi.org/10.1029/2011GL049089, 2011b.

440 Salmanidou, D. M., Beck, J., and Guillas, S.: Probabilistic, high-resolution tsunami predictions in North Cascadia by exploiting sequential design for efficient emulation, Natural Hazards and Earth System Sciences Discussions, pp. 1–24, https://doi.org/https://doi.org/10.5194/nhess-2021-63, 2021.

Satake, K., Nishimura, Y., Putra, P. S., Gusman, A. R., Sunendar, H., Fujii, Y., Tanioka, Y., Latief, H., and Yulianto, E.: Tsunami source of the 2010 Mentawai, Indonesia earthquake inferred from tsunami field survey and waveform modeling, Pure and Applied Geophysics, 170,
445 1567–1582, https://doi.org/https://doi.org/10.1007/s00024-012-0536-y, 2013.

Shinagawa, H., Tsugawa, T., Matsumura, M., Iyemori, T., Saito, A., Maruyama, T., et al.: Two-dimensional simulation of ionospheric variations in the vicinity of the epicenter of the Tohoku-oki earthquake on 11 March 2011, Geophysical Research Letters, 40, 5009–5013, https://doi.org/https://doi.org/10.1002/2013GL057627, 2013.

Tanioka, Y. and Gusman, A. R.: Near-field tsunami inundation forecast method assimilating ocean bottom pressure
450 data: A synthetic test for the 2011 Tohoku-oki tsunami, Physics of the Earth and Planetary Interiors, 283, 82–91, https://doi.org/https://doi.org/10.1016/j.pepi.2018.08.006, 2018.

Tsugawa, T., Saito, A., Otsuka, Y., Nishioka, M., Maruyama, T., Kato, H., et al.: Ionospheric disturbances detected by GPS total electron content observation after the 2011 off the Pacific coast of Tohoku Earthquake, Earth, planets and space, 63, 875–879, https://doi.org/https://doi.org/10.5047/eps.2011.06.035, 2011.

455 Wächter, J., Babeyko, A., Fleischer, J., Häner, R., Hammitzsch, M., Kloth, A., and Lendholt, M.: Development of tsunami early warning systems and future challenges, Natural Hazards and Earth System Sciences, 12, 1923–1935, https://doi.org/https://doi.org/10.5194/nhess-12-1923-2012, 2012.

Wang, Y., Maeda, T., Satake, K., Heidarzadeh, M., Su, H., Sheehan, A., and Gusman, A.: Tsunami data assimilation without a dense observation network, Geophysical Research Letters, 46, 2045–2053, https://doi.org/https://doi.org/10.1029/2018GL080930, 2019.

460 Zettergren, M. and Snively, J.: Latitude and Longitude Dependence of Ionospheric TEC and Magnetic Perturbations From Infrasonic-Acoustic Waves Generated by Strong Seismic Events, Geophysical Research Letters, 46, 1132–1140, https://doi.org/https://doi.org/10.1029/2018GL081569, 2019.

Zettergren, M., Snively, J., Komjathy, A., and Verkhoglyadova, O.: Nonlinear ionospheric responses to large-amplitude infrasonic-acoustic waves generated by undersea earthquakes, Journal of Geophysical Research: Space Physics, 122, 2272–2291,
465 https://doi.org/https://doi.org/10.1002/2016JA023159, 2017.